ACS APPLIED MATERIALS & INTERFACES

Research Article

www.acsami.org

General Reagent Free Route to pH Responsive Polyacryloyl Hydrazide Capped Metal Nanogels for Synergistic Anticancer Therapeutics

Rewati Raman Ujjwal,[†] Mahaveer Prasad Purohit,[‡] Satyakam Patnaik,*[,‡] and Umaprasana Ojha*[,†]

[†]Department of Chemistry, Rajiv Gandhi Institute of Petroleum Technology, Ratapur Chowk, Rae Bareli UP-229316, India

[‡]Academy of Scientific and Innovative Research, CSIR-IITR, Lucknow, CSIR-IITR Campus, Lucknow 226001, India

Supporting Information

ABSTRACT: Herewith, we report a facile synthesis of pH responsive polyacryloyl hydrazide (PAH) capped silver (Ag) or gold (Au) nanogels for anticancer therapeutic applications. A cost-effective instant synthesis of PAH-Ag or PAH-Au nanoparticles (NPs) possessing controllable particle diameter and narrow size distribution was accomplished by adding $AgNO_3$ or AuCl to the aqueous solution of PAH under ambient conditions without using any additional reagent. PAH possessing carbonyl hydrazide pendant functionality served as both reducing and capping agent to produce and stabilize the NPs. The stability analysis by UV−vis, dynamic light scattering, and transmission electron microscopy techniques suggested that these NPs may be stored in a refrigerator for at least up to 2 weeks with negligible change in conformation. The average hydrodynamic size of PAH-Ag NPs synthesized using 0.2 mmol/L $AgNO_3$ changed from 122 to 226 nm on changing the pH of the medium from 5.4 to 7.4, which is a characteristic property of pH responsive nanogel. Camptothecin (CPT) with adequate loading efficiency (6.3%) was encapsulated in the PAH-Ag nanogels. Under pH 5.4 conditions, these nanogels released 78% of the originally loaded CPT over a period of 70 h. The antiproliferative potential of PAH-Ag-CPT nanogels (at [CPT] = 0.6 μg/mL) against MCF-7 breast adenocarcinoma cells were ∼350% higher compared to that of the free CPT as evidenced by high cellular internalization of these nanogels. Induction of apoptosis in MCF-7 breast adeno-carcinoma cells by PAH-Ag-CPT nanogels was evidenced by accumulation of late apoptotic cell population. Drug along with the PAH-Ag NPs were also encapsulated in a pH responsive hydrogel through in situ gelation at room temperature using acrylic acid as the cross-linker. The resulting hydrogel released quantitative amounts of both drug and PAH-Ag NPs over a period of 16 h. The simplicity of synthesis and ease of drug loading with efficient release render these NPs a viable candidate for various biomedical applications, and moreover this synthetic procedure may be extended to other metal NPs.

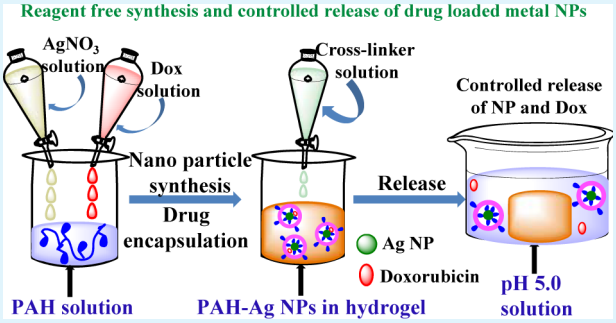

KEYWORDS: *metal nanoparticles, nanomedicine, controlled release, polyacryloyl hydrazide, nanogels, apoptosis*

INTRODUCTION

Synthesis and surface grafting of metal nanoparticles (NPs) have garnered huge interest in recent times due to their useful antimicrobial properties,[1,2] catalytic activities in the form of a reducing/oxidizing agent,[3,4] electrical and thermal conductivity,[5] and optical properties.[6,7] Owing to the preceding interesting properties, silver (Ag) or gold (Au) NPs have found applications as sensors,[8] catalysts in redox reactions,[9] electronic devices, and antimicrobial agents.[10,11] For example, Lewis and co-workers used poly(acrylic acid) capped Ag NPs to successfully print flexible microelectrodes.[12]

Ag and Au NPs are particularly favorable for various biomedical applications due to their useful antibacterial and antiviral properties.[13,14] The biocidal activities of bare Ag NPs, though interesting, are associated with potential toxicity toward cells due to release of Ag cations from Ag NPs.[15] Therefore, efforts were made to immobilize Ag NPs into a biocompatible material, typically a polymer matrix or small molecular capping agent to resist oxidation.[16,17] For various medical applications, polymeric capping agents were preferred over their low molecular weight analog such as sodium citrate, since the later is known to possess unfavorable anticoagulant activity.[18] The polymer matrix further helped by releasing the Ag NPs in a controlled manner to achieve desired bactericidal effect and avoid eukaryotic toxicity.[19,20] Another problematic aspect of traditional Ag NP synthetic procedure is the use of inorganic or organic reducing agents.[21] The biocompatibility of the resulting Ag NPs containing a trace amount of these toxic impurities is questionable.[22] Therefore, the focus has shifted to the development of benign and green procedures involving

Received: March 20, 2015
Accepted: May 11, 2015
Published: May 11, 2015

DOI: 10.1021/acsami.5b02452
ACS Appl. Mater. Interfaces 2015, 7, 11497−11507

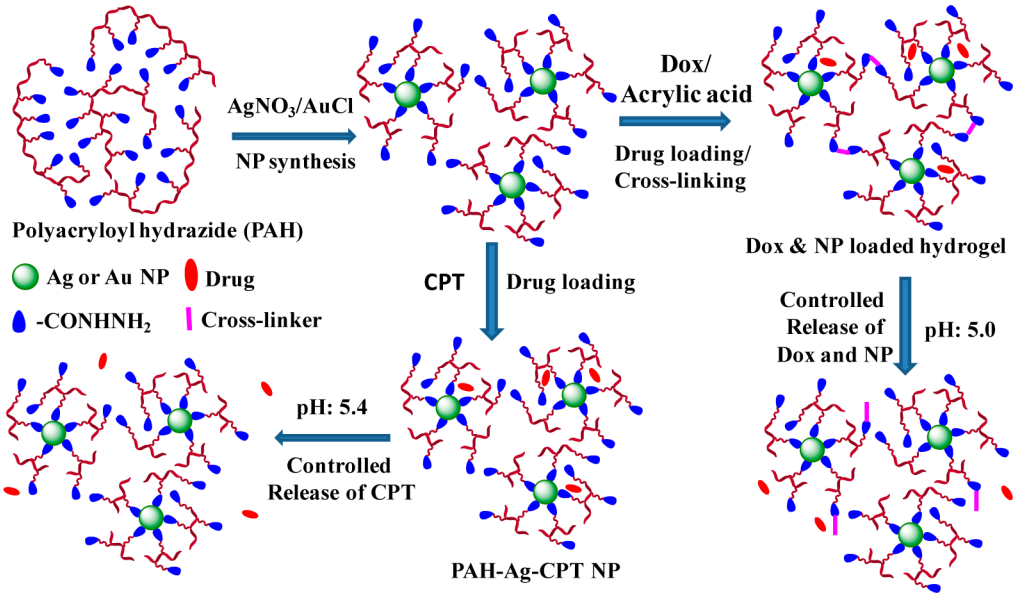

Figure 1. Schematic illustration of PAH-Ag NP formation and drug encapsulation followed by controlled release.

polymeric reagents to synthesize the NPs for various biomedical applications.[23,24] For example, polyamines were used as nanoreactors to synthesize NPs due to their efficient capping ability.[25,26] However, an additional agent ($NaBH_4$) or source (UV) was utilized for reduction of metal ions. The above analysis suggests, new synthetic procedures based on only polymeric reducing and capping agents would be highly beneficial for future applications.

The role of hydrazine as an effective reducing agent for various functional groups is well documented in literature.[27] A range of materials based on polyacryloyl hydrazide (PAH) have already been reported for various biomedical applications.[28] Recently, we have proposed a simple and cost-effective procedure to synthesize PAH possessing hydrazide functionality in each repeating unit.[29] The motive behind selecting PAH for the synthesis of metal NPs is multifold. PAH would serve as the reducing agent for the metal ion precursors. The $-NH_2$ group present in the pendant hydrazide moiety may swiftly cap the surface and stabilize the resulting NPs.[30] The presence of hydrophilic PAH on the surface would assist easy dispersibility of Ag NPs in aqueous media. More importantly, the presence of PAH (pH ≈ 8.7) on the surface of Ag NPs may resist the oxidation of Ag^0 to Ag^+ and thereby reduce the toxicity associated with Ag NPs.[31] The pH responsiveness of PAH may be swiftly utilized to encapsulate various drug molecules in the NPs and release them in a controlled manner under physiological conditions. Development of polymer coated metal NPs for controlled release applications carries a huge potential in biological systems.[32] PAH also forms cytocompatible, injectable, and stimuli responsive hydrogels with a range of cross-linkers.[33] Therefore, the procedure may be extended to encapsulate the synthesized Ag NPs along with drug molecules in situ through formation of hydrogels. Overall, PAH is envisaged to promote a reagent free synthesis of stable and nontoxic Ag NPs with the added advantage of encapsulating and releasing drugs in a controlled manner as schematically shown in Figure 1.

Compiling the preceding aspects, a cost-effective and reagent free synthesis of PAH-Ag or Au NPs with controllable particle diameter is described in this report. The stability of the synthesized NPs is studied using UV−vis spectroscopic, dynamic light scattering (DLS), and transmission electron microscopy (TEM) characterization techniques. Various drug loading procedures are discussed. The antiproliferative effect of these drug loaded PAH-Ag NPs on MCF-7 cells is demonstrated.

EXPERIMENTAL SECTION

Materials. Methyl acrylate (SD Fine Chemicals, >99%), potassium bromate (Merck, >99.0%), sodium hydrogen sulfite (Merck, 58.5−67.4%), acrylic acid (AA, Merck, >99.0%), sodium chloride (NaCl, Qualigens, >99.9%), hydrazine hydrate (SD Fine Chemicals, 99%), tetra-*n*-butylammonium bromide (TBAB, Merck, ≥98.0), silver nitrate (Qualigens, 99%), camptothecin (CPT, Sigma Alrich, HPLC grade), doxorubicine (Dox, Sigma-Aldrich), acrylic acid (Merck, 58.5−67.4%), HNO_3 (Qualigens, >99.9%), $HClO_4$ (Qualigens, >99.9%), AuCl (Fisher Scientific), 1,4-dioxane (SD Fine Chemicals, 99%), trifloroacetic acid (Sigma-Aldrich), dialysis bag [SMALL WONDER LYZER (10−12 kDaA)], acetonitrile (ACN, Sigma Alrich, HPLC grade), rhodamine B isothiocynate (RITC, Sigma Alrich, 95%), dimethyl sulfoxide (DMSO, SRL), 4′,6-diamidino-2-phenylindole (DAPI, Sigma Alrich, 98%), FITC Annexin V apoptosis detection kit (BD Pharmingen), methanol (Qualigens, >99.9%), sodium acetate (Merck, >99.0%), glacial acetic acid (Qualigens, >99.9%), disodium hydrogen phosphate (Merck, >99.0%), and potassium dihydrogen phosphate (Merck, >99.0%) were used without further purification. Tetrahydrofuran (THF, Qualigens, 99.0%) was refluxed over sodium metal and benzophenone overnight and distilled under a nitrogen atmosphere prior to use.

Instrumentation. The PerkinElmer Spectrum Two FT-IR spectrometer was used to record the FT-IR spectra of the samples as either solid or thin films. All of the samples were recorded using "attenuated total reflectance" (ATR) mode. The PIKE MIRacle single reflection horizontal ATR accessory equipped with ZnSe ATR crystal was used for recording the spectra. Lab India UV−Vis 3200 was used to record the UV−vis spectra of the sample. Samples were recorded at room temperature with a 1 nm/s scan rate over the wavelength range from 250 to 700 nm.

The size distribution curves of the particles present in the solutions were measured by DLS approach using a Zetasizer Nano-ZS (Malvern) equipped with green laser (523 nm). The intensity of the scattered light was detected at the angle of 173°. For each sample, five measurements were performed. The data processing was carried out

DOI: 10.1021/acsami.5b02452
ACS Appl. Mater. Interfaces 2015, 7, 11497−11507

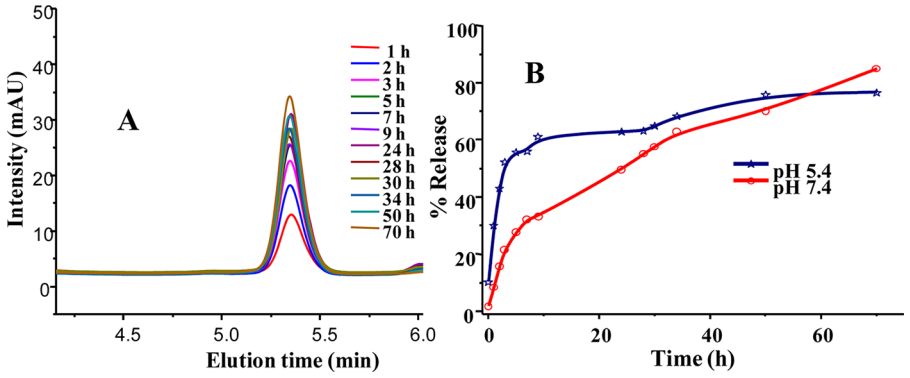

Figure 2. (A) HPLC traces showing gradual release of CPT at pH = 5.4 and (B) release profile of CPT at pH 5.4 and 7.4 from PAH-Ag-CPT NPs as determined from HPLC analysis.

using the Zetasizer software 6.20 (Malvern Instruments). The as-synthesized PAH-Ag NPs were dialyzed, centrifuged, and re-dispersed in Milli-Q water by sonication prior to the scan. The size distributions were reported as volume and number distributions.

Field-emission scanning electron microscopic (FESEM) images were recorded using a Carl Zeiss-Sigma field-emission microscope operating at an acceleration voltage of 3 kV. Samples were prepared by drop-casting PAH-Ag NPs on silver foil. The samples were sputtered with gold before recording the images.

High resolution transmission electron microscope (HR-TEM) images were recorded using FEI Technai G2 F20 operated at 200 kV with a magnification of $6 \times 10^6\times$ and resolution of 0.2 Å. For TEM, a JEM-200CX transmission electron microscope operated at 200 kV was utilized. The specimens were prepared by drop-casting the suspension of PAH-Ag NPs on a copper grid coated with transparent graphite. The water was evaporated at room temperature prior to recording the images.

A Waters Associates (Milford, MA, USA) Model ALC 244 instrument for high performance liquid chromatography (HPLC) equipped with a PDA detector was used for monitoring the release of drug at 254 nm from the PAH-Ag matrix. A Waters Associates Bondapak C-18 cm × 3.9 mm column was used for this purpose. Solvent delivery and mixing were accomplished by interfacing the twin M6000A pumps to the Model 660 solvent programmer. An acetonitrile and 0.1% TFA water mixture was used as the mobile phase.

To determine the silver contents in PAH-Ag NPs, an AAS ZEEnit 700 atomic absorption spectroscope (AAS) was employed. For calibration, a series of aqueous solutions of $AgNO_3$ with concentrations in the range of 1−5 ppm were utilized. HNO_3:$HClO_4$ = 6:1 was used as the leaching agent to digest organic components out of the PAH-Ag nanocomposite. All measurements were carried out in an air acetylene flame. For calibration purposes, the absorbance value at 328 nm was used. The sample total volumes were made up to 50 mL by using water before recording the spectra. The data presented were the average of two measurements.

Synthesis of PAH. A solution of PMA (5.0 g, 0.08 mmol) in 150 mL of THF was placed in a 1 L round-bottom flask. To it hydrazine hydrate (19.4 g, 0.4 mol) and TBAB (5.0 g, 15.5 mmol) was added. The mixture was stirred at 60 °C for 12 h. The reaction mixture was cooled to room temperature and kept undisturbed until the layers separated out. The aqueous layer was transferred into methanol to precipitate the product polymer. The obtained white product was washed with methanol several times to remove the low molecular weight impurities and dried under reduced pressure at ambient temperature. Yield: 4.6 g, 91%. ^{1}H NMR (500 MHz, D_2O; ppm): δ 1.3−2.2 (m, 3H, -CH_2−CH−CO-), 3.15 (br, 2H, -CONH−NH_2). FT-IR (thin film, cm^{-1}): 981 (m, C−N), 1447 (m, C−H), 1607 (s, C═O), 2924 (m, C−H), 3261 (m, N−H).

Synthesis of PAH-Ag NPs. A typical synthetic procedure is described as follows. To an aqueous solution of PAH (25 mL, 2% (w/v)), $AgNO_3$ solution (250 μL, 20 mmol/L) was added at room temperature and the mixture was stirred for 30 min. The color of the solution turned to light yellow suggesting PAH-Ag NP formation. The aqueous dispersion of PAH-Ag NP was then dialyzed for 24 h to remove unreacted starting materials. The solution was then centrifuged to isolate the resulting NPs. The final product was dried by lyophilization prior to characterization unless otherwise mentioned.

Synthesis of PAH-Au NPs. To an aqueous solution of PAH (25 mL, 2% (w/v)), AuCl solution (250 μL, 50 mmol/L in dioxane) was added at 10 °C and the mixture was stirred for 10 min. The color of the solution turned to light purple suggesting PAH-Au NP formation. The aqueous dispersion of PAH-Au NP was then dialyzed for 24 h to remove unreacted starting materials. The solution was then centrifuged to isolate the resulting NPs. The final product was dried by lyophilization prior to characterization unless otherwise mentioned.

Preparation of Dox and PAH-Ag NP Encapsulated Hydrogel. PAH-Ag NP was synthesized by adding $AgNO_3$ (0.4 mmol/L) to the aqueous solution of PAH (2.0 mL, 30% (w/v)) at room temperature. To the yellow colored NP solution, Dox (1.0 mg, 1.83 μmol) was added and the mixture was stirred for 5 min at room temperature. To the preceding mixture, acrylic acid (0.4 g, 5.6 mmol) was added as cross-linker and the red colored solution was kept undisturbed at room temperature for 3 h to prepare the hydrogel.

Release of Dox and PAH-Ag NP from pH Responsive Hydrogel. The Dox and PAH-Ag NP encapsulated hydrogel was immersed in the pH 5.0 solution. The temperature of the solution was maintained at 37 °C. After selected time intervals, the UV−vis spectroscopic analysis of the media was recorded. The percent release was quantified by comparing the absorbance of the media after different time intervals to that of the known initial concentration of Dox.

Synthesis of PAH-Ag-CPT NPs. Powdered PAH-Ag NP (40 mg) was dispersed in 10 mL of Milli-Q water (pH = 7.4 or 5.4), and to it a THF solution (2 mL) of CPT (4 mg, 11.5 μmol) was added in a dropwise manner with constant stirring. The mixture was then stirred at room temperature for 12 h. The resulting mixture was dialyzed for 4 h using a SMALL WONDER LYZER (10−12 kDaA) dialysis bag. The dialyzed CPT encapsulated PAH-Ag NPs were centrifuged at 12500 rpm for 20 min to separate free CPT. The final CPT loaded PAH-Ag NPs were dried by lyophilization for further studies.

Loading Efficiency of PAH-Ag-CPT NPs. A mixture of PAH-Ag-CPT NPs (1.0 mg) and THF (10 mL) was kept in the incubator at 37 °C for 4 h to disperse the NPs. The UV−vis spectroscopic analysis of the dispersion was recorded. The amount of loaded CPT (W_l) was determined from the absorbance using a standard calibration curve. The loading efficiency was then determined using the following equation:

$$\text{loading efficiency} = \frac{w_l}{w_{NP}} \times 100 \quad (1)$$

where w_{NP} is the total amount of PAH-Ag NPs used for encapsulation.

Similarly, entrapment efficiency was determined from the following equation;

DOI: 10.1021/acsami.5b02452
ACS Appl. Mater. Interfaces 2015, 7, 11497−11507

Scheme 1. Synthesis of PAH-Ag NPs, Drug Encapsulation, and Hydrogel Formation

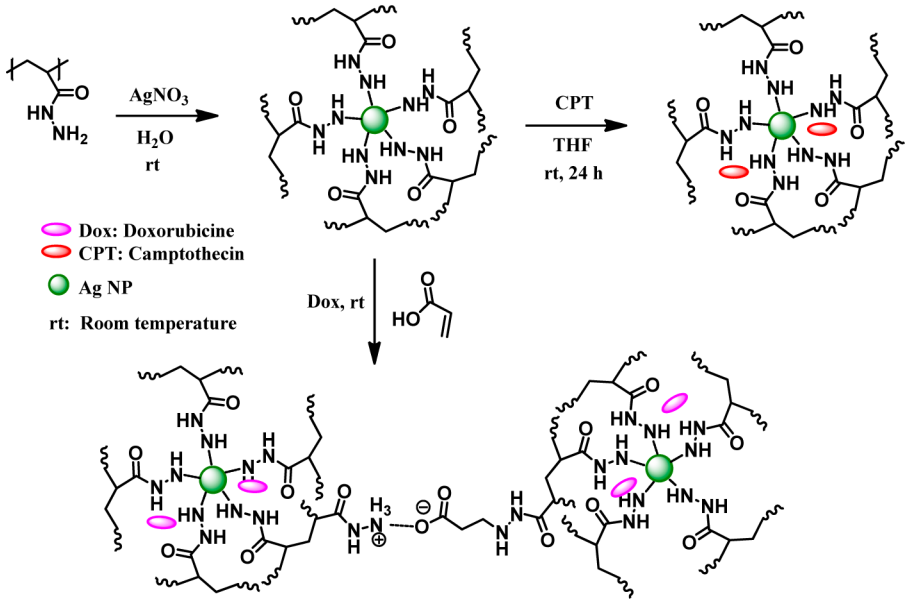

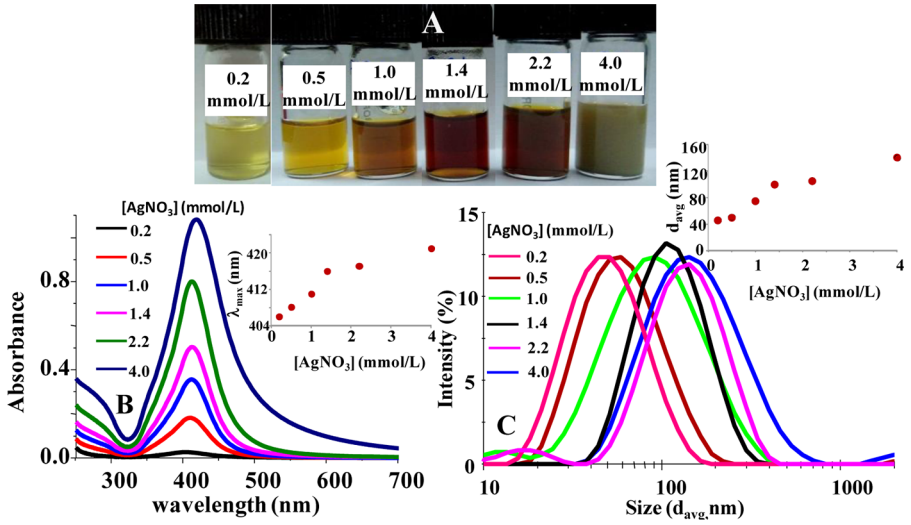

Figure 3. (A) Color, (B) UV−vis spectra (after diluting the original reaction mixtures by 40 times), and (C) DLS traces of PAH-Ag NPs synthesized using various concentrations of $AgNO_3$ and 0.02 g/mL of PAH. Insets for B and C show the λ_{max} versus [$AgNO_3$] and d_{av} versus [$AgNO_3$] plots, respectively, of PAH-Ag NPs synthesized using different concentrations of $AgNO_3$.

$$\text{entrapment efficiency} = \frac{w_l}{w_t} \times 100 \quad (2)$$

where w_t is the total amount of CPT used for encapsulation.

Controlled Release of CPT from PAH-Ag-CPT NPs. The PAH-Ag-CPT NPs were taken in the dialysis bag and dipped in 10 mL of pH 7.4 or 5.4 buffer solution. The temperature of the medium was maintained at 37 °C with constant stirring. HPLC analysis of the aliquots collected after predetermined time intervals were recorded to determine the extent of release (Figure 2A,B). A mixture of acetonitrile and 0.1% TFA water was used as the mobile phase, and the flow rate was maintained at 0.8 mL/min for the HPLC studies. The integration of peak at the retention time of 5.3 min was used to quantify the release.

Cell Viability Assay. The anticancer property of the PAH-Ag-CPT NPs against MCF-7 breast adeno-carcinoma cells was determined by 3-(4,5-dimethylthiazol-2-yl)-2,5-diphenyltertrazolium bromide (MTT) assay. Cells were plated at 70−80% confluence and incubated at 37 °C under a humidified atmosphere with CO_2 (5%) for 24 h. For treatment exposure, the cells were incubated with PAH-Ag NPs (1−10 μg/mL), CPT (6.3% of 1−10 μg/mL), or PAH-Ag-CPT NPs (1−10 μg/mL). After incubation for 24 and 48 h, the modified NP exposed cells were washed with PBS, and then MTT (10 μL, 5 mg/mL) was added into each well. The cells were incubated for an additional 4 h, followed by removal of media and addition of 100 μL of DMSO into each well to dissolve insoluble formazan formed by the mitochondrial dehydrogenase in live cells. After 30 min of gentle shaking, the absorbance of dissolved formazan was measured using a FLUOstar Omega microplate reader (BMG LABTECH) at 530 nm. The cell viability was expressed as the percentage of live cells relative to the control. All experiments were performed in triplicate, and the data were presented as the averaged results with standard deviation.

Statistical Analysis. All data are presented as the mean ± standard deviation (SD), and a p-value of <0.05 was considered statistically significant. The difference between three or more groups was analyzed by one-way ANOVA multiple comparisons.

Fluorescent Labeling of PAH-Ag NPs with Rhodamine B Isothiocyanate. RITC labeled PAH-Ag NPs were prepared by following a method described elsewhere.[34] A solution of RITC in DMSO (1 μg/mL) was added to an aqueous suspension of PAH-Ag

DOI: 10.1021/acsami.5b02452
ACS Appl. Mater. Interfaces 2015, 7, 11497−11507

NPs (25 mg) at pH 8 in a dropwise manner. The resulting mixture was stirred for 24 h in the dark. Thereafter, RITC labeled PAH-Ag NPs were dialyzed against a DMSO:H_2O (10:90 (v/v)) mixture for 24 h to remove the unreacted dye. Finally the resulting PAH-Ag-RITC NPs were lyophilized and used for subsequent studies.

***In Vitro* Cellular Uptake of Fluorescent Labeled PAH-Ag NPs.** For qualitative analysis of cellular uptake, the harvested MCF-7 cells were seeded on 18 mm coverslips in a 12 well culture plate at a density of 5×10^4 cells/well and incubated overnight for cell attachment. Attached cells were incubated with 50 μg/mL of RITC labeled PAH-Ag NPs over different time periods at 37 °C in a CO_2 incubator. Thereafter, cells on coverslips were washed with PBS to remove the free NPs outside of the cells. Washed cells were fixed with chilled methanol at 4 °C for 30 min. Nuclei were stained with DAPI (1 mg/mL) and observed under a Nikon fluorescence microscope equipped with a camera.

Annexin V-FITC/PI Apoptosis Assay. Cellular apoptosis induced by PAH-Ag-CPT NPs in MCF-7 cells was evaluated by using Annexin V-FITC/propidium iodide (PI) double stain binding assay as per the manufacturer's instructions (Becton Dickinson, Franklin Lakes, NJ, USA). Briefly cells were seeded at a density of 2×10^5 cells/well in 6 well plates and allowed to attach for 24 h. Thereafter, the medium of the culture was replaced with media containing different concentrations (1, 2.5, 5, 7.5, and 10 μg/mL) of PAH-Ag-CPT NPs and incubated for another 24 h in a CO_2 incubator at 37 °C. Following incubation, cells were trypsinized, centrifuged at 300*g* for 5 min and repeatedly washed with PBS. The cell pellet was suspended in 100 μL of 1X Annexin V binding buffer in a FACS tube followed by the addition of Annexin V-FITC (5 μL) and propidium iodide (5 μL), and incubated for 15 min at room temperature in the dark. Before FACS analysis, 400 μL of 1X Annexin V binding buffer was added in the FACS tube and the cells were analyzed using a Flow Cytometer (BD-LSR). 10,000 events were acquired though Annexin V (FL- 1, 530 nm) versus PI (FL-2, 585 nm) dot plot and the data analyzed by CellQuest software.

RESULTS AND DISCUSSION

PAH with M_n = 62000 and PDI = 1.6 was synthesized and purified as reported elsewhere.[29] The synthetic procedure for PAH-Ag NPs followed by hydrogel formation is illustrated in Scheme 1. The PAH-Ag NPs were synthesized by adding different concentrations (0.2−4.0 mmol/L) of $AgNO_3$ to 0.02 g/mL aqueous solution of PAH (pH ≈ 8.7) at room temperature. The hydrazide functionality present in PAH served as both reducing agent for $AgNO_3$ and surface capping agent of the resulting NPs.

The formation of Ag NPs was swift under ambient conditions, and a characteristic yellow color of the reaction mixture appeared within ~15 min of the addition of 0.2 mmol/L $AgNO_3$ (Figure 3A). The UV−vis spectrum of the preceding reaction mixture displayed a λ_{max} at ~406 nm, which is similar to that of the polymer capped Ag NPs reported earlier (Figure 3B).[35] The color of the reaction mixture gradually changed from yellow to brown upon increasing the concentration of $AgNO_3$ in the solution suggesting a possible change in particle size. The surface plasmon band was typically observed in the range of 406−421 nm for samples synthesized using various concentrations (0.2−4.0 mmol/L) of $AgNO_3$, and the absorbance gradually increased with [$AgNO_3$] (Figure 3B). A bathochromic shift in the λ_{max} of the NP solution was noticed with increase in [$AgNO_3$], which could be attributed to a possible gradual increase in the average particle size of the resulting PAH-Ag NPs (inset, Figure 3B).[36] A relatively narrow full width at half-maximum (fwhm) ≈ 42−68 nm for the

Table 1. Particle size, Silver Content, and Surface Charge of PAH-Ag NPs

[$AgNO_3$] (mmol/L)	d_{av} (nm)[a]	Ag (wt %)[b]	ζ (mV)[a]	PDI[a]	fwhm (nm)[c]
0.2	45.7	0.3	−26.9	0.4	42
0.5	50.4	2.5	−26.3	0.4	60
1.0	75.0	3.1	−22.4	0.4	62
1.4	100.1	5.9	−24.5	0.3	67
2.2	105.9	6.2	−24.9	0.2	68
4.0	140.9	8.5	−31.2	0.3	83

[a]The average particle diameter (d_{av}), PDI, and ζ potential were determined from DLS analysis. [b]The weight percent of Ag in PAH-Ag NP was determined from AAS analysis. [c]The fwhm was determined from UV−vis spectroscopic analysis.

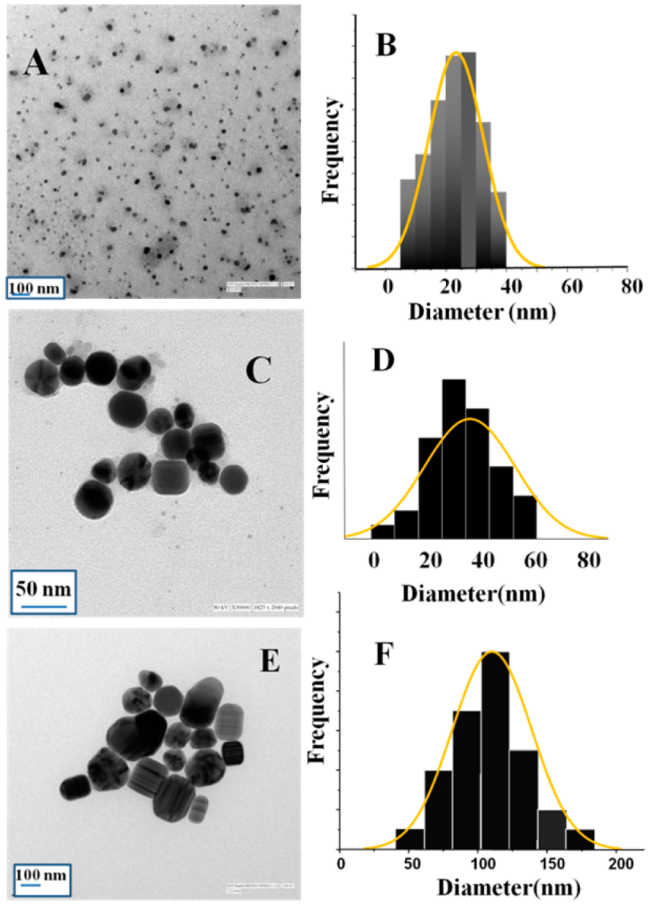

Figure 4. HRTEM images and particle size distributions of PAH-Ag NPs synthesized using and 0.02 g/mL of PAH and (A and B) 0.2, (C and D) 0.5, and (E and F) 2.2 mmol/L $AgNO_3$.

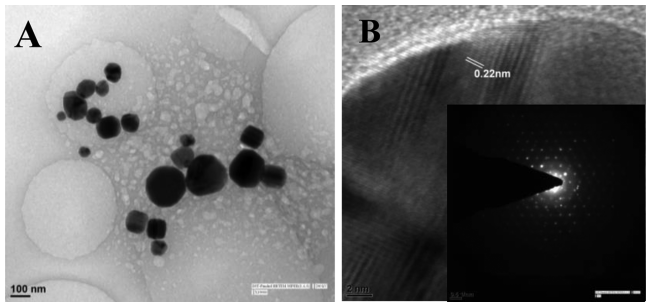

Figure 5. (A) HRTEM image and (B) diffraction pattern of PAH-Ag NPs synthesized using 4.0 mmol/L $AgNO_3$ and 0.02 g/mL PAH.

DOI: 10.1021/acsami.5b02452
ACS Appl. Mater. Interfaces 2015, 7, 11497−11507

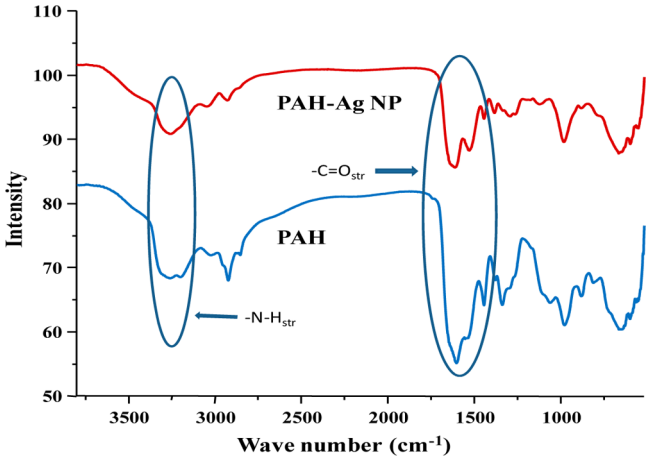

Figure 6. ATR FT-IR spectra of PAH and PAH-Ag NPs.

samples synthesized using 0.2−2.2 mmol/L $AgNO_3$ suggested the particle size distribution was reasonably controlled (Table 1). The particle size, morphology, and uniformity of size distribution were further determined by HRTEM, DLS, and FESEM analysis. The NPs synthesized using 0.2 mmol/L $AgNO_3$ were mostly spherical, and the particle diameters were in the range of 8−35 nm (Figure 4A). The size distribution was considerably narrow, with the particles possessing diameters in the range of 20−30 nm being the most abundant ones (Figure 4B). FESEM images also displayed clusters of NPs possessing size distribution similar to that of the HRTEM data (Supporting Information (SI) Figure S1).

As anticipated, the average size of NPs increased with the increase in the amount of $AgNO_3$ in the reaction mixture. The average sizes of the PAH-Ag NPs synthesized using 0.5 and 2.2 mmol/L $AgNO_3$ were ∼32 and ∼120 nm, respectively (Figure 4C−F and SI Figure S2). Interestingly, the NPs synthesized using higher concentrations of $AgNO_3$ (1.0−4.0 mmol/L) were of mixed morphology. Triangular, cubical, and hexagonal particles were also visible along with the spherical ones (SI Figure S3). The possibility of shape control of the resulting Ag NPs using the concentration or molecular weight of PAH as the tool is currently explored as a separate project. However, the control over polydispersity was compromised to some extent, when the NPs were synthesized using a very high concentration (4.0 mmol/L) of $AgNO_3$. The sizes of the resulting PAH-Ag NPs were distributed over a range of 40−200 nm (Figure 5A). The electron diffraction pattern suggested packing of crystalline Ag NPs into a face centered cubic lattice with a typical lattice fringe of 2.2 Å as reported earlier (Figure 5B).[37]

The as-synthesized PAH-Ag NPs were centrifuged to remove the unassociated PAH present in the solution and re-dispersed in water before DLS analysis. The size distribution traces of PAH-Ag NPs synthesized using various concentrations of $AgNO_3$ are shown in Figure 3C. The average particle diameter (d_{av}) of the PAH-Ag NPs gradually increased with an increase in [$AgNO_3$] (inset, Figure 3C). The d_{av} of NPs synthesized using 0.2−4.0 mmol/L $AgNO_3$ were observed in the range of 45−140 nm (Table 1).

The PDIs of the NPs were in the range of 0.2−0.4 suggesting reasonably narrow size distribution. In some compositions, the presence of a minor peak in the range of 1−20 nm, possibly due to the formation of uncapped Ag NPs in small proportions, affected the overall PDI to some extent. The average particle sizes obtained from the DLS studies were somewhat higher than those of the data (25−130 nm) obtained from TEM analysis (SI Figure S4). This could be attributed to the apparent hydrodynamic volume of the PAH-Ag NPs in solution.[38] Importantly, the UV−vis spectroscopic, TEM, and DLS data suggested that particles with predetermined sizes may be synthesized by controlling the ratio of $AgNO_3$:PAH in the reaction mixture. The FT-IR spectrum of the purified and lyophilized PAH-Ag NPs displayed characteristic bands at 1620 and 3253 cm^{-1} for -C═O$_{str}$ and -C−N$_{str}$, respectively, due to the presence of PAH on the surface of Ag NPs (Figure 6). A band at 365 cm^{-1} accountable to Ag−N$_{str}$ was also observed supporting the surface capping of Ag NPs (SI Figure S5). AAS analysis revealed the presence of a substantial amount (91.5−

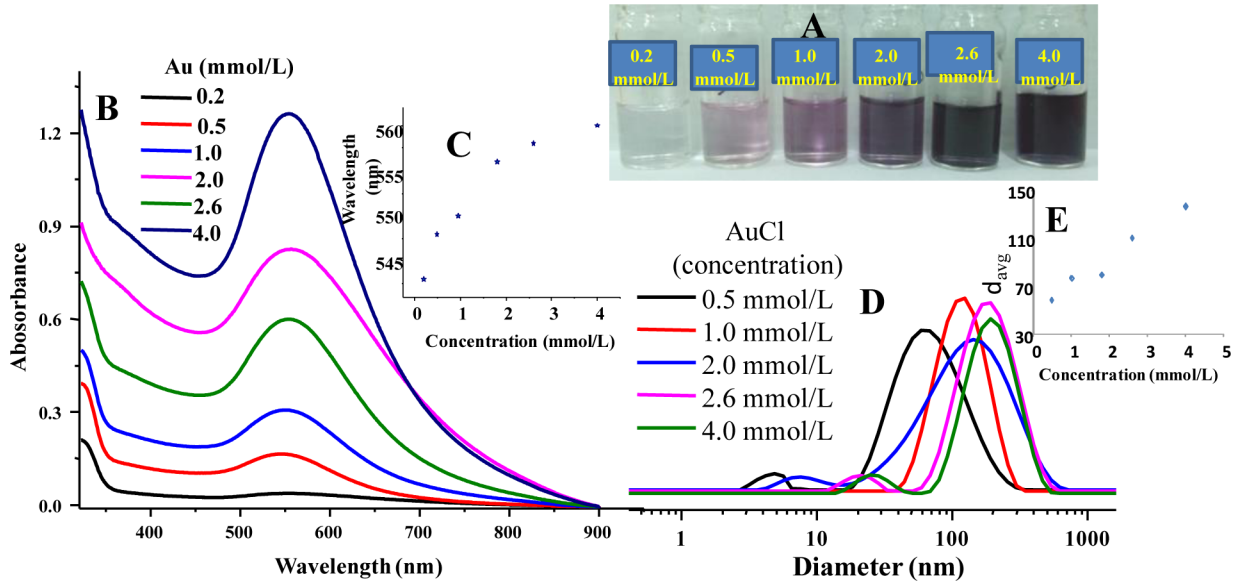

Figure 7. (A) Color, (B) UV−vis traces, and (D) DLS traces of the PAH-Au NPs synthesized using various concentrations of AuCl. Panels C and E represent the absorption maximum versus [AuCl] and average particle size (d_{av}) versus [AuCl] plots of PAH-Au NPs, respectively.

DOI: 10.1021/acsami.5b02452
ACS Appl. Mater. Interfaces 2015, 7, 11497−11507

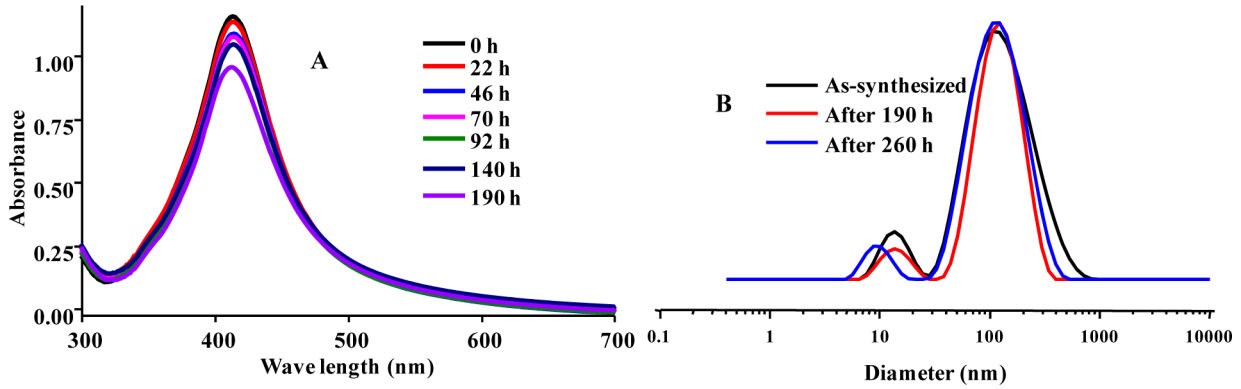

Figure 8. Effect of aging on absorbance (A) and average particle sizes (B) of PAH-Ag NPs synthesized using 0.2 mmol/L $AgNO_3$ and 0.02 g/mL PAH.

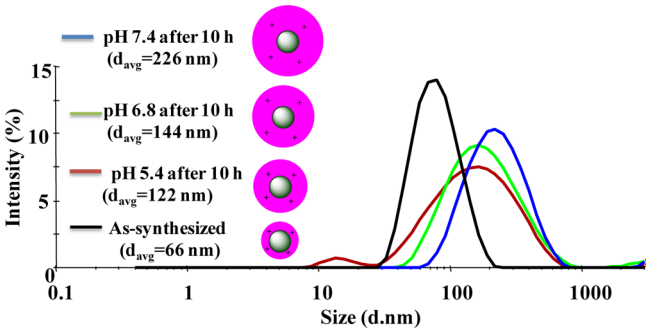

Figure 9. DLS traces of PAH-Ag NPs incubated for 10 h under different pH conditions.

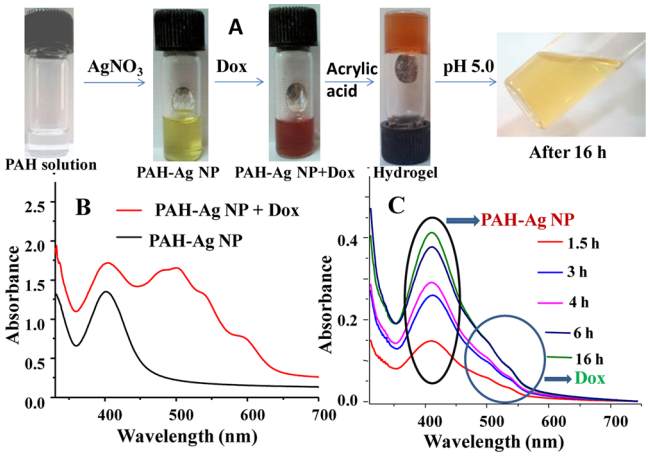

Figure 10. (A) Visual observation of NP formation, Dox loading, and hydrogel formation, (B) UV−vis spectra of the PAH-Ag NP and Dox loaded PAH-Ag NP, and (C) gradual release of PAH-Ag NP and Dox from hydrogel.

99.7%) of organic constituents in the NPs further illustrating the formation of PAH-Ag NPs (Table 1).

Synthesis of PAH-Au NPs. Synthesis of PAH-Au NPs was attempted using a procedure similar to that of the PAH-Ag NPs. The temperature (10 °C) in this particular case was maintained below room temperature due to the involvement of a reactive Au salt (AuCl). The color of the reaction mixture changed to light purple within 5 min of the addition of AuCl suggesting formation of PAH-Au NPs. The intensity of the color gradually increased on increasing the concentration of AuCl in the reaction mixture (Figure 7A). Characteristic surface plasmon bands for the resulting PAH-Au NPs were observed in the range of 540−560 nm, which is similar to that of the polymer capped Au NPs reported in the literature (Figure 7B).[39] The gradual increase in λ_{max} with an increase in [AuCl] could be due to a possible increase in particle size (Figure 7C). Similarly, the d_{av} (68−137 nm) obtained from DLS studies were dependent on the concentration (0.5−4.0 mmol/L) of AuCl in the reaction mixture (Figure 7E).

The fwhms (75−90 nm) calculated from the UV−vis traces and PDIs (0.3−0.5) obtained from the DLS traces suggested a reasonably narrow size distribution of particles for all compositions of PAH-Au NPs. However, fairly small peaks in the range of 5−10 nm suggested that unprotected Au NPs in minute amount may have formed during the process (Figure 7D). TEM images of the PAH-Au NPs synthesized using 0.5 and 1.0 mmol/L AuCl displayed uniform distribution of particles with sizes in the narrow range of 10−30 and 30−60 nm, respectively (SI Figures S6 and 7). The preceding study suggested that the synthetic procedure could also be utilized for preparation of size controlled PAH-Au NPs and may be extended to the synthesis of other PAH capped metal NPs.

Stability of PAH-Ag NPs. The ζ potentials (surface charge of the NPs) of PAH-Ag NPs were observed in the range of −22 to −30 mV suggesting moderate stability of the PAH-Ag NPs, as reported in the literature for various polymer capped Ag NPs (Table 1).[40] To further ascertain the stability, PAH-Ag NPs in aqueous dispersion were stored at 5 °C and any possible conformational changes were monitored after regular time intervals via UV−vis, DLS, and TEM analysis. The NPs in aqueous dispersion retained more than 90% of the original absorbance (λ_{max} = 410 nm) up to 190 h, and the shape of the UV−vis trace remained unaltered suggesting negligible loss in conformation (Figure 8). No noticeable change in the d_{av} of PAH-Ag NPs was observed in the DLS analysis up to 260 h (Figure 8B). Similarly, the TEM data displayed distribution of PAH-Ag NPs with minimal segregation after 14 days (SI Figure S8). The preceding study suggested these NPs in aqueous dispersion may be stored in a refrigerator for at least up to 12 days with negligible loss in conformation.

pH responsiveness of the PAH-Ag NPs. The PAH-Ag or Au NPs were presumed to be pH responsive owing to the presence of PAH on the metal NP surface. To examine the effect of pH, PAH-Ag NPs were incubated under different pH (5.4, 6.8, and 7.4) conditions for ∼10 h and d_{av} were compared with that (66 nm) of the as synthesized sample (Figure 9). The PAH-Ag NPs displayed typical characteristics of pH responsive

DOI: 10.1021/acsami.5b02452
ACS Appl. Mater. Interfaces 2015, 7, 11497−11507

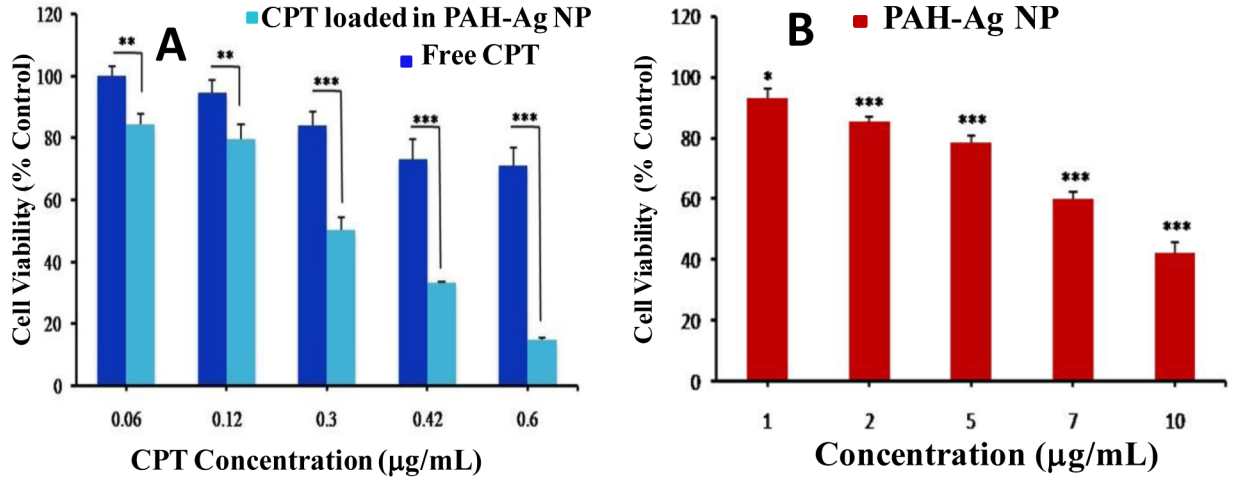

Figure 11. (A) Difference between viability inhibition potential of CPT loaded PAH-Ag NPs and free CPT against MCF-7 cells and (B) viability inhibition potential of PAH-Ag NP against MCF-7 cells. The vertical bars represent the mean ± SD, n = 3 (number of experiments per concentration). Single asterisk (*) represents $p < 0.05$, double asterisks (**) represent $p < 0.01$, and triple asterisks (***) $p < 0.001$, and a p-value of <0.05 was considered statistically significant.

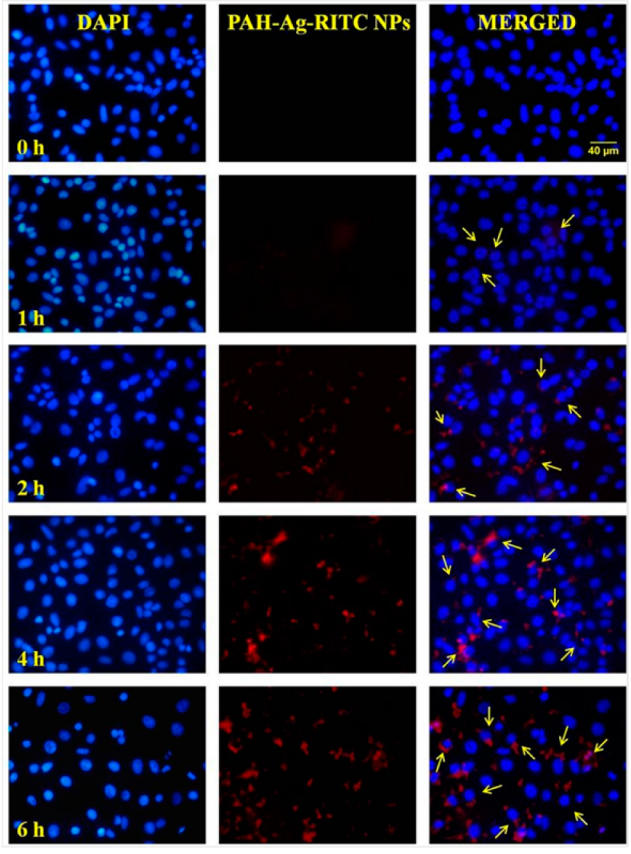

Figure 12. Fluorescence microscopic images of intracellular uptake of PAH-Ag-RITC NPs in MCF-7 cells after regular time intervals.

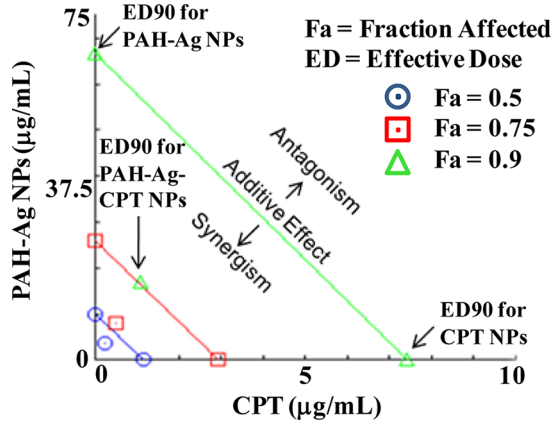

Figure 13. Synergism analysis of PAH-Ag-CPT NPs. The isobologram represents the synergistic effect of PAH-Ag NPs and CPT in PAH-Ag-CPT NPs at different doses (ED90, ED75, and ED50). The isobologram was generated by using Compusyn software.

nanogel by swelling controllably under different pH conditions. Under neutral (pH = 7.4) conditions, the d_{av} of PAH-Ag NPs increased by 340%, whereas under pH 5.4 conditions the d_{av} increased by ∼180% only compared to that of the as-synthesized samples. The preceding could be attributed to the protonation of -NH_2 moieties present in the PAH chain to the corresponding -NH_3^+ ions under acidic conditions. The hydrogen bond forming capacity of -NH_3^+ is expected to be lower compared to that of the -NH_2 due to the loss of lone pair on "N", which may have affected the water content and therefore the swelling of the PAH-Ag NPs. However, no significant effect of temperature in the range of 25−50 °C on d_{av} was noticed. The above controlled swelling of PAH-Ag NPs induced by pH was utilized to encapsulate and release various antitumor drugs. Overall, the current approach allowed a much faster synthesis of stable, size tunable, and pH responsive PAH capped Ag or Au NPs under ambient conditions compared to those of the recently reported procedures in aqueous solution under elevated conditions.[41,42]

Drug Encapsulation. Two approaches were followed to load antitumor drugs into the PAH-Ag NP matrix. In the first approach, both drug (Dox) and PAH-Ag NPs were encapsulated into a pH responsive hydrogel through in situ cross-linking. Dox was chosen as the drug in this particular case, as the presence of -$CONHNH_2$ functionality in PAH provided the opportunity to load the drug by both chemical (through formation of acid labile hydrazone linkage) attachment and physical (through hydrogel formation) encapsulation.[43,44] In this particular case, physical encapsulation and release of Dox

DOI: 10.1021/acsami.5b02452
ACS Appl. Mater. Interfaces 2015, 7, 11497−11507

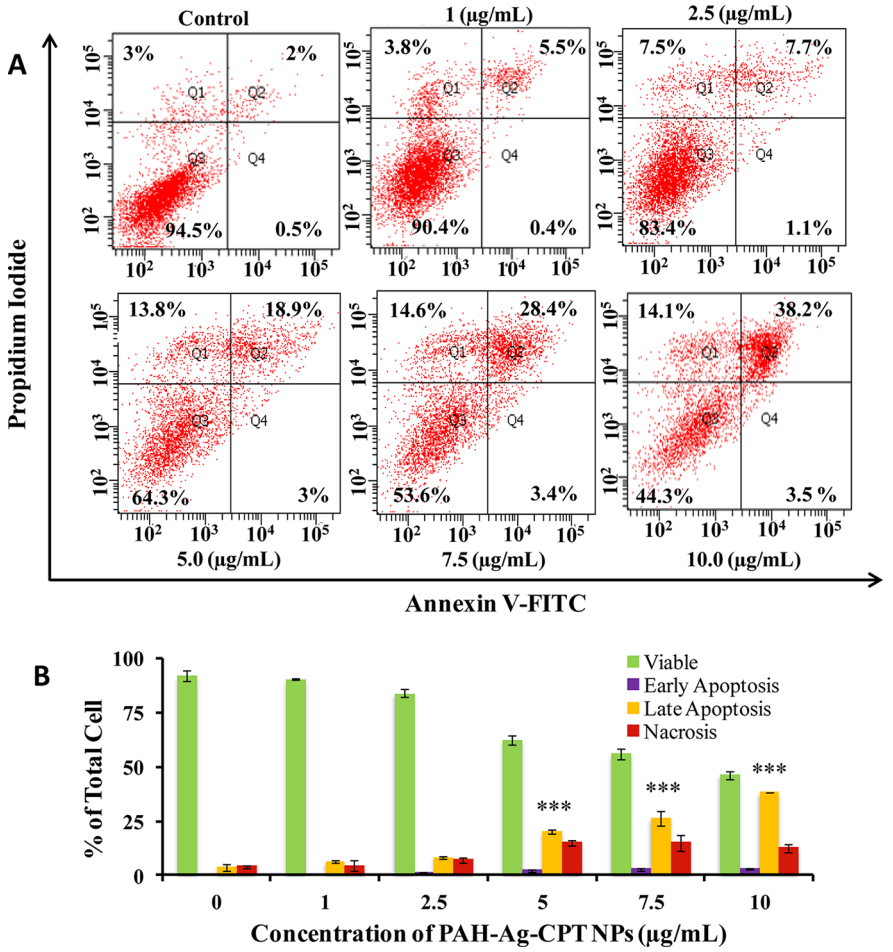

Figure 14. Flow cytometric analysis of PAH-Ag-CPT NPs (1, 2.5, 5, 7.5, and 10 μg/mL) induced apoptosis in MCF-7 cells after 24 h of incubation using Annexin V-FITC/PI method. (A) Results expressed as a dot plot representing one of three independent experiments: lower left (LL), live cells (Annexin V^-/PI^-); lower right (LR), early/primary apoptotic cells (Annexin V^+/PI^-); upper right (UR), late/secondary apoptotic cells (Annexin V^+/PI^+); upper left (UL), necrotic cells (Annexin V^-/PI^+). "X-axes" represent the concentrations of PAH-Ag-CPT NPs. (B) Cell distribution after 24 h of incubation with different concentrations of PAH-Ag-CPT NPs. The data represent mean ± SD of three independent experiments. Three asterisks (***) indicate $p < 0.001$ as compared to the control, using one-way ANOVA.

along with PAH-Ag NPs has been demonstrated as a proof of principle. A suitable cross-linker (AA) was used to prepare the hydrogel at room temperature through a physical cross-linking procedure reported by us recently.[33] The yellow colored PAH-Ag NP solution changed to red after addition of Dox (Figure 10A).

UV−vis spectroscopic analysis supported the presence of both PAH-Ag NPs and Dox by displaying peaks around 406 and 500 nm, respectively (Figure 10B). Gelation occurred after 3 h of the addition of AA. The release was monitored at pH 5.0 after regular time intervals (Figure 10C). The absorbance of peaks at 406 nm accountable to Ag NP and the set of peaks around 500 nm accountable to Dox increased with time, suggesting release of both NP and Dox from hydrogel matrix (Figure 10C). Quantitative release of Dox occurred over a period of 16 h as the hydrogel became liquid like due to substantial dissociation of physical cross-linking (Figure 10A).

In the second approach, Dox was loaded into the PAH-Ag NPs ($d_{av} \approx 46$ nm) in solution to prepare PAH-Ag-Dox NPs. However, owing to poor loading efficiency (~2.3%) of Dox in the PAH-Ag NPs, a relatively hydrophobic and planar drug (CPT) was chosen. Interestingly, the hydrophobic drug entrapment (62.5%) and loading efficiencies (6.3%) improved significantly under neutral (pH = 7.4) conditions compared to that of the Dox. However, both the loading (1.2%) and entrapment efficiency (11.8%) of CPT under acidic (pH = 5.4) conditions substantially decreased. The release of CPT was then monitored at pH 5.4 (found to be in tumor microenvironment) and 7.4 by HPLC analysis.[45] Under both pH conditions, an initial burst release was noticed in the first 10 h of incubation followed by a gradual release up to 70 h. A maximum release of ~85% occurred in pH 7.4 solution, whereas the release was limited to ~78% in pH 5.4 (Figure 2B). The inferior loading and release of CPT under pH 5.4 conditions compared to that of the pH 7.4 could be attributed to the higher swelling of PAH-Ag NPs in the case of the later (Figure 9).

In order to assess the efficacy of PAH-Ag-CPT NPs, the antiproliferative effect of these NPs on MCF-7 breast adenocarcinoma cells was evaluated using MTT assay. Moreover, we evaluated the inhibitory concentration (IC_{50}) by constructing a dose−response curve of CPT loaded Ag-nanogels and PAH-Ag NPs on MCF-7 cells. As shown in Figure 11, PAH-Ag-CPT NPs (CPT concentration = 0.06−0.6 μg/mL) significantly inhibited the proliferation of MCF-7 breast adeno-carcinoma cells (84−15%) in a dose-dependent manner (~ IC_{50} = 5.0 μg/

DOI: 10.1021/acsami.5b02452
ACS Appl. Mater. Interfaces 2015, 7, 11497−11507

mL). In contrast to the PAH-Ag-CPT NPs, PAH-Ag NPs (5 μg/mL) and CPT (0.3 μg/mL) exhibited lower inhibitory rates (79% and 84%, respectively) on MCF-7 (Figure 11A,B). However, no dose-dependent response for PAH NPs was noticed against MCF-7 cells (SI Figure S9).To achieve nanogel-based anticancer therapeutic effect, the nanogels absorbed into cancer cells must attain a relatively high level of concentration. Further, the cellular uptake of PAH-Ag NPs (50 μg/mL) was time dependent and the increased localization of RITC tagged PAH-Ag NPs within the cytosols of MCF-7 cells was visible in the confocal images (Figure 12).

To understand the interaction of drug (CPT) with PAH-Ag NPs and to elucidate their combinatorial effect in PAH-Ag-CPT NPs, we analyzed the synergism by studying the antiproliferative effects of the preceding individual components at various dose concentrations using Compusyn software in MCF7 cells.[46,47] The isobologram analysis revealed that the antiproliferative effects of the preceding two components in PAH-Ag-CPT NPs was synergistic as evidenced by the presence of data points below the line of additive effect (Figure 13). The ratio of the PAH-Ag NPs and CPT in PAH-Ag-CPT NPs was also synergistically effective at different dose concentrations (ED_{90}, ED_{75}, and ED_{50}). Moreover, the combination index value of the ED_{50} of PAH-Ag-CPT NPs was 0.58309, which further confirmed the synergism between CPT and PAH-Ag NPs.

Apoptosis is a genetically programmed process that is of paramount importance during embryonic development, as well as in maintenance of tissue homeostasis, under pathological conditions. Cell apoptosis was further confirmed by Annexin V-FITC/PI double staining and analyzed by flow cytometry. In the untreated control sample, the majority (94.5%) of cells were viable and nonapoptotic. With increases in doses of CPT loaded PAH-Ag NPs, the Annexin V^-/PI^- population gradually decreased and cells undergoing late apoptosis (Annexin V^+/PI^+) increased. As the concentration of CPT loaded PAH-Ag NPs increased (1−10 μg/mL), the percentage of the MCF-7 apoptosis cells significantly increased (5.5−38.2%) compared to that of the control (Figure 14A). At higher doses, an increase in Annexin V^-/PI^+ population was observed indicating dead or necrotic cells. Figure 14B represents the cell distribution after 24 h of incubation with different concentrations of PAH-Ag-CPT NPs, where cells are in late apoptotic stage.

These preliminary results suggest, there may be a synergistic effect between the PAH-Ag NP carrier and the drug. Detailed studies on the action of PAH-Ag-CPT NPs on various mammalian cells are under progress. These PAH-Ag-drug NPs are promising candidates for various therapeutic applications. Furthermore, the loading and release kinetics may be tailored depending upon the suitability of use.

CONCLUSION

Stable PAH capped Ag or Au NPs with predetermined particle size may be synthesized at room temperature without using any additional reagent. These NPs exhibit responsive nanogel characteristics and are suitable candidates for targeted delivery application. Various antitumor drugs may be encapsulated in a PAH-Ag NP matrix and released in a controlled manner for various biomedical applications. These PAH-Ag−drug nanogels exhibit significantly higher antiproliferative effect on MCF-7 cells and are promising candidates for various anticancer therapeutic applications. These NPs along with drugs may also be trapped inside an injectable hydrogel for controlled release applications. The whole process of NP synthesis and drug loading can be conducted in a single pot and does not warrant any postpurification procedure. Surface engineering of these NPs is currently under progress to further enhance their efficiency against tumor cells.

ASSOCIATED CONTENT

Supporting Information

FESEM images and HRTEM images of PAH-Ag NPs, FT-IR spectra of PAH-Ag NPs, particle size comparison plot, pH response data, stability data, and inhibition data of PAH NPs. The Supporting Information is available free of charge on the ACS Publications website at DOI: 10.1021/acsami.5b02452.

AUTHOR INFORMATION

Corresponding Authors

*(U.O.) E-mail: uojha@rgipt.ac.in. Tel.: 0535-270-4221. Fax: 0535-221-1888.

*(S.P.) E-mail: satyakampatnaik@iitr.res.in. Tel.: 0522-2963827. Fax: 0522-2628227.

Notes

The authors declare no competing financial interest.

ACKNOWLEDGMENTS

Department of Science and Technology, New Delhi, India (Grant SERB/F/5311/2012-13) is acknowledged for providing partial financial assistance for the project. S.P. acknowledges the funding support by CSIR—12th 5 year network project, NanoSHE, Nanomaterials: Applications and Impact on Safety, Health and Environment.

REFERENCES

(1) Kumar, A.; Vemula, P. K.; Ajayan, P. M.; John, G. Silver-Nanoparticle Embedded Antimicrobial Paints Based on Vegetable Oil. *Nat. Mater.* **2008**, *7*, 236−241.

(2) Li, X.; Robinson, S. M.; Gupta, A.; Saha, K.; Jiang, Z.; Moyano, D. F.; Sahar, A.; Riley, M. A.; Rotello, V. M. Functional Gold Nanoparticles as Potent Antimicrobial Agents against Multi-Drug-Resistant Bacteria. *ACS Nano* **2014**, *8*, 10682−10686.

(3) Cuenya, B. R. Metal Nanoparticle Catalysts Beginning to Shape-up. *Acc. Chem. Res.* **2013**, *46*, 1682−1691.

(4) Linic, S.; Christopher, P.; Xin, H.; Marimuthu, A. Catalytic and Photocatalytic Transformations on Metal Nanoparticles with Targeted Geometric and Plasmonic Properties. *Acc. Chem. Res.* **2013**, *46*, 1890−1899.

(5) Putnam, S. A.; Cahill, D. G.; V. Braun, P. V. Thermal Conductivity of Nanoparticle Suspensions. *J. Appl. Phys.* **2006**, *99*, No. 084308-1.

(6) Jin, R.; Cao, Y. W.; Mirkin, C. A.; Kelly, K. L.; Schatz, G. C.; Zheng, J. G. Photoinduced Conversion of Silver Nanospheres to Nanoprisms. *Science* **2001**, *294*, 1901−1903.

(7) Xia, X.; Zeng, J.; Otejen, L. K.; Li, Q.; Xia, Y. Quantitative Analysis of the Role Played by Poly(vinylpyrrolidone) in Seed-Mediated Growth of Ag Nanocrystals. *J. Am. Chem. Soc.* **2012**, *134*, 1793−1801.

(8) Taton, T. A.; Mirkin, C. A.; Letsinger, R. L. Scanometric DNA Array Detection with Nanoparticle Probes. *Science* **2000**, *289*, 1757−1760.

(9) Dotzauer, D. M.; Dai, J.; Sun, L.; Bruening, M. L. Catalytic Membranes Prepared Using Layer-by-Layer Adsorption of Polyelectrolyte/Metal Nanoparticle Films in Porous Supports. *Nano Lett.* **2006**, *6*, 2268−2272.

(10) Ma, R.; Kwon, S.; Zheng, Q.; Kwon, H. Y.; Kim, J. I.; Choi, H. R.; Baik, S. Carbon-Nanotube/Silver Networks in Nitrile Butadiene

DOI: 10.1021/acsami.5b02452
ACS Appl. Mater. Interfaces 2015, 7, 11497−11507

Rubber for Highly Conductive Flexible Adhesives. *Adv. Mater.* **2012**, *24*, 3344−3349.
(11) Xia, X.; Zeng, J.; Zhang, Q.; Moran, C. M.; Xia, Y. Recent Developments in Shape-Controlled Synthesis of Silver Nanocrystals. *J. Phys. Chem. C* **2012**, *116*, 21647−21656.
(12) Ahn, B. Y.; Duoss, E. B.; Motala, M. J.; Guo, X.; Park, S.; Xiong, Y.; Yoon, J.; Nuzzo, R. G.; Rogers, J. A.; Lewis, J. A. Omnidirectional Printing of Flexible, Stretchable, and Spanning Silver Microelectrodes. *Science* **2009**, *323*, 1590−1593.
(13) Xiu, Z.; Zhang, Q.; Puppala, H. L.; Colvin, V. L.; Alvarez, P. J. Negligible Particle-Specific Antibacterial Activity of Silver Nanoparticles. *Nano Lett.* **2012**, *12*, 4271−4275.
(14) Fasciani, C.; Silvero, M. J.; Anghel, M. A.; Argüello, G. A.; Becerra, C. M.; Scaiano, J. C. Aspartame-Stabilized Gold−Silver Bimetallic Biocompatible Nanostructures with Plasmonic Photothermal Properties, Antibacterial Activity, and Long-Term Stability. *J. Am. Chem. Soc.* **2014**, *136*, 17394−17397.
(15) George, S.; Lin, S.; Ji, Z.; Thomas, C. R.; Li, L. J.; Mecklenburg, M.; Meng, H.; Wang, X.; Zhang, H.; Xia, T.; Hohman, J. N.; Lin, S.; Zink, J. L.; Weiss, P. S.; Nel, A. E. Surface Defects on Plate-Shaped Silver Nanoparticles Contribute to Its Hazard Potential in a Fish Gill Cell Line and Zebrafish Embryos. *ACS Nano* **2012**, *6*, 3745−3759.
(16) AshaRani, P. V.; Mun, G. L. K.; Hande, M. P.; Valiyaveettil, S. Cytotoxicity and Genotoxicity of Silver Nanoparticles in Human Cells. *ACS Nano* **2009**, *3*, 279−290.
(17) Eby, D. M.; Schaeublin, N. M.; Farrington, K. E.; Hussain, S. M.; Johnson, G. R. Lysozyme Catalyzes the Formation of Antimicrobial Silver Nanoparticles. *ACS Nano* **2009**, *3*, 984−994.
(18) Ocwieja, M.; Adamczyk, Z. Controlled Release of Silver Nanoparticles from Monolayers Deposited on PAH Covered Mica. *Langmuir* **2013**, *29*, 3546−3555.
(19) Zhu, Y.; Morisato, K.; Li, W.; Kanamori, K.; Nakanishi, K. Synthesis of Silver Nanoparticles Confined in Hierarchically Porous Monolithic Silica: A New Function in Aromatic Hydrocarbon Separations. *ACS Appl. Mater. Interfaces* **2013**, *5*, 2118−2125.
(20) Liu, J. Y.; Sonshine, D. A.; Shervani, S.; Hurt, R. H. Controlled Release of Biologically Active Silver from Nanosilver Surfaces. *ACS Nano* **2010**, *4*, 6903−6913.
(21) Raveendran, P.; Fu, J.; Wallen, S. L. Completely Green Synthesis and Stabilization of Metal Nanoparticles. *J. Am. Chem. Soc.* **2003**, *125*, 13940−13941.
(22) Shen, Z.; Luo, Y.; Wang, Q.; Wang, X.; Sun, R. High-Value Utilization of Lignin to Synthesize Ag Nanoparticles with Detection Capacity for Hg^{2+}. *ACS Appl. Mater. Interfaces* **2014**, *6*, 16147−16155.
(23) Li, B.; Smilgies, D. M.; Price, A. D.; Huber, D. L.; Clem, P. G.; Fan, H. Poly(*N*-isopropylacrylamide) Surfactant-Functionalized Responsive Silver Nanoparticles and Superlattices. *ACS Nano* **2014**, *8*, 4799−4804.
(24) Zhou, B.; Zheng, L.; Peng, C.; Li, D.; Li, J.; Wen, S.; Shen, M.; Zhang, G.; Shi, X. Synthesis and Characterization of PEGylated Polyethylenimine-Entrapped Gold Nanoparticles for Blood Pool and Tumor CT Imaging. *ACS Appl. Mater. Interfaces* **2014**, *6*, 17190−17199.
(25) Chia, K. K.; Cohen, R. E.; Rubner, M. F. Amine-Rich Polyelectrolyte Multilayer Nanoreactors for in Situ Gold Nanoparticle Synthesis. *Chem. Mater.* **2008**, *20*, 6756−6763.
(26) Dai, J.; Bruening, M. L. Catalytic Nanoparticles Formed by Reduction of Metal Ions in Multilayered Polyelectrolyte Films. *Nano Lett.* **2002**, *2*, 497−501.
(27) Wei, X.-W.; Zhu, G.-X.; Liu, Y.-J.; Ni, Y.-H.; Song, Y.; Xu, Z. Large-Scale Controlled Synthesis of FeCo Nanocubes and Microcages by Wet Chemistry. *Chem. Mater.* **2008**, *20*, 6248−6253.
(28) Godula, K.; Bertozzi, C. R. Synthesis of Glycopolymers for Microarray Applications via Ligation of Reducing Sugars to a Poly(acryloyl hydrazide) Scaffold. *J. Am. Chem. Soc.* **2010**, *132*, 9963−9965.
(29) Kumar, A.; Ujjwal, R. R.; Mittal, A.; Bansal, A.; Ojha, U. Polyacryloyl Hydrazide: An Efficient, Simple, and Cost Effective Precursor to a Range of Functional Materials through Hydrazide Based Click Reactions. *ACS Appl. Mater. Interfaces* **2014**, *6*, 1855−1865.
(30) He, Y.; Liu, D.; He, X.; Cui, H. One-Pot Synthesis of Luminol Functionalized Silver Nanoparticles with Chemiluminescence Activity for Ultrasensitive DNA Sensing. *Chem. Commun. (Cambridge, U. K.)* **2011**, *47*, 10692−10694.
(31) Monchi, M.; Berghmans, D.; Ledoux, D.; Canivet, J. L.; Dubois, B.; Damas, P. Citrate vs. Heparin for Anticoagulation in Continuous Venovenous Hemofiltration: A Prospective Randomized Study. *Intensive Care Med.* **2004**, *30*, 260−265.
(32) Yavuz, M. S.; Cheng, Y.; Chen, J.; C, M.; Zhang, Q.; Rycenga, M.; Xie, J.; Kim, C.; Song, K. H.; Schwartz, A. G.; Wang, L. V.; Xia, Y. Gold Nanocages Covered by Smart Polymers for Controlled Release with Near-Infrared Light. *Nat. Mater.* **2009**, *8*, 935−939.
(33) Kumar, A.; Samal, S. K.; Dash, R.; Ojha, U. Polyacryloyl Hydrazide Based Injectable & Stimuli Responsive Hydrogels with Tunable Properties. *J. Mater. Chem. B* **2014**, *2*, 7429−7439.
(34) Das, M.; Mishra, D.; Dhak, P.; Gupta, S.; Maiti, T. K.; Basak, A.; Pramanik, P. Biofunctionalized, Phosphonate-Grafted, Ultrasmall Iron Oxide Nanoparticles for Combined Targeted Cancer Therapy and Multimodal Imaging. *Small* **2009**, *5*, 2883−2893.
(35) Alarcon, E. I.; Udekwu, K.; Skog, M.; Pacioni, N. L.; Stamplecoskie, K. G.; Béjar, M. G.; Polisetti, N.; Wickham, A.; Dahlfors, R. A.; Griffith, M.; Scaiano, J. C. The Biocompatibility and Antibacterial Properties of Collagen-Stabilized, Photochemically Prepared Silver Nanoparticles. *Biomaterials* **2012**, *33*, 4947−4956.
(36) Agnihotri, S.; Mukherji, S.; Mukherji, S. Size-Controlled Silver Nanoparticles Synthesized Over the Range 5−100 nm Using the Same Protocol and Their Antibacterial Efficacy. *RSC Adv.* **2014**, *4*, 3974−3983.
(37) Germain, V.; Li, J.; Ingert, D.; Wang, Z. L.; Pileni, M. P. Stacking Faults in Formation of Ag Nanodisks. *J. Phys. Chem. B* **2003**, *107*, 8717−8720.
(38) Palma, R. D.; Peeters, S.; Bael, M. J. V.; Rul, H. V.; Bonroy, K.; Laureyn, W.; Mullens, J.; Borghs, G.; Maes, G. Silane Ligand Exchange to Make Hydrophobic Superparamagnetic Nanoparticles Water-Dispersible. *Chem. Mater.* **2007**, *19*, 1821−1831.
(39) Hamner, K. L.; Maye, M. M. Thermal Aggregation Properties of Nanoparticles Modified with Temperature Sensitive Copolymers. *Langmuir* **2013**, *29*, 15217−15223.
(40) Schneid, A. C.; Roesch, E. W.; Sperb, F.; Matte, U.; Silveira, N. P.; Costa, T. M. H.; Benvenuti, E. V.; Menezes, E. W. Silver Nanoparticle−Ionic Silsesquioxane: A New System Proposed as an Antibacterial Agent. *J. Mater. Chem. B* **2014**, *2*, 1079−1086.
(41) Liang, M.; Su, R.; Huang, R.; Qi, W.; Yu, Y.; Wang, L.; He, Z. Facile in Situ Synthesis of Silver Nanoparticles on Procyanidin-Grafted Eggshell Membrane and Their Catalytic Properties. *ACS Appl. Mater. Interfaces* **2014**, *6*, 4638−4649.
(42) Sharma, S.; Sanpui, P.; Chattopadhyay, A.; Ghosh, S. S. Fabrication of Antibacterial Silver Nanoparticle—Sodium Alginate−Chitosan Composite Films. *RSC Adv.* **2012**, *2*, 5837−5843.
(43) Makssimenko, A.; Dosio, F.; Mougin, J.; Ferrero, A.; Wack, S.; Reddy, L. H.; Weyn, A. A.; Lepeltier, E.; Bourgaux, C.; Stella, B.; Cattel, L.; Couvreur, P. A Unique Squalenoylated and Nonpegylated Doxorubicin Nanomedicine with Systemic Long-Circulating Properties and Anticancer Activity. *Proc. Natl. Acad. Sci. U. S. A.* **2014**, *111*, E217−E226.
(44) Boyer, C.; Whittaker, M. R.; Bulmus, V.; Liu, J.; Davis, T. P. The Design and Utility of Polymer-Stabilized Iron-Oxide Nanoparticles for Nanomedicine Applications. *NPG Asia Mater.* **2010**, *2*, 23−30.
(45) Helmlinger, G.; Schell, A.; Dellian, M.; Forbes, N. S.; Jain, R. K. Acid Production in Glycolysis-Impaired Tumors Provides New Insights into Tumor Metabolism. *Clin. Cancer Res.* **2002**, *8*, 1284−1291.
(46) Chou, T. C. Drug Combination Studies and Their Synergy Quantification Using the Chou-Talalay Method. *Cancer Res.* **2010**, *70*, 440−446.
(47) Tallarida, R. J. Drug Synergism: Its Detection and Applications. *J. Pharmacol. Exp. Ther.* **2001**, *298*, 865−872.

DOI: 10.1021/acsami.5b02452
ACS Appl. Mater. Interfaces 2015, 7, 11497−11507